ACS APPLIED MATERIALS & INTERFACES

Research Article

www.acsami.org

Synthesis of Nestlike ZnO Hierarchically Porous Structures and Analysis of Their Gas Sensing Properties

Xinzhen Wang,[†] Wei Liu,[‡] Jiurong Liu,*[,†] Fenglong Wang,[†] Jing Kong,[†] Song Qiu,[†] Cuizhu He,[†] and Liqiang Luan[‡]

[†]Key Laboratory for Liquid−Solid Structural Evolution and Processing of Materials, Ministry of Education and School of Materials Science and Engineering, Shandong University, Jinan, Shandong 250061, People's Republic of China

[‡]State Key Laboratory of Crystal Materials, Shandong University, Jinan 250100, People's Republic of China

ABSTRACT: Nestlike 3D ZnO porous structures with size of 1.0−3.0 μm have been synthesized through annealing the zinc hydroxide carbonate precursor, which was obtained by a one-pot hydrothermal process with the assistance of glycine, Na_2SO_4, and polyvinyl pyrrolidone (PVP). The nestlike 3D ZnO structures are built of 2D nanoflakes with the thickness of ca. 20 nm, which exhibit the nanoporous wormhole-like characteristic. The measured surface area is 36.4 m^2g^{-1} and the pore size is ca. 3−40 nm. The unique nestlike 3D ZnO porous structures provided large contacting surface area for electrons, oxygen and target gas molecules, and abundant channels for gas diffusion and mass transport. Gas sensing tests showed that the nestlike 3D ZnO porous structures exhibit excellent gas sensing performances such as high sensitivity and fast response and recovery speed, suggesting the potential applications as advanced gas sensing materials.

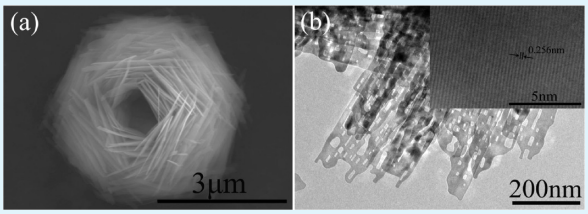

KEYWORDS: *zinc oxide, nanoporous, nestlike structures, gas sensing, hydrothermal method*

INTRODUCTION

Porous materials with various morphologies have attracted remarkable attention because porous materials with high porosity and specific surface area usually exhibit unique physical properties different from solid structures, which make them critically important in technological applications such as photo catalysts,[1] gas sensors,[2,3] Li-ion battery electrodes,[4,5] solar cells,[6,7] and so on.[8−11] Zinc oxide, a functional wide band gap (ca. 3.37 eV) n-type semiconductor, has been extensively investigated due to its special optical and electrical properties, which provide wide potential applications in gas sensors,[12] piezoelectric and photoelectric nanodevices,[13−18] solar cells,[19,20] light-emitting devices,[21−24] photocatalysts,[25,26] and laser emission.[27] In addition, ZnO nanostructures also have great potential to be used in the structural nanocomposites.[28,29] Various ZnO nanostrctures such as one-dimensional (1D) nanorods,[30] nanowires,[31] nanotubes,[32] and nanoneedles,[33] two-dimensional (2D) nanobelts[34] and nanosheets,[35] and three-dimensional (3D) brushlike,[36] flowerlike,[37,38] hollow architectures,[39] etc., have been synthesized and their properties have been investigated. Comparing with 1D and 2D nanostructures, 3D hierarchical architectures assembling from 1D or 2D nanosized building blocks probably show unique properties different from that of building blocks, leading to the functionality enhancement of 3D hierarchical architectures.[40,41] Recently, porous ZnO nano/microstructures have also drawn extensive research attention due to their porous structured networks and high internal surface area, which result in the enhancement of gas sensing,[42] lithium-ion battery,[43] selective adsorption,[44] photoluminescence,[45,46] photovoltaic,[47] and photocatalytic properties.[48,49] Specifically, the introduction of pores into ZnO nano/microstructures facilitates the gas diffusion and mass transport, enormously improving gas sensor performance.[50]

Wet chemical procedures combining with calcination processes have been widely employed to synthesize porous ZnO nano/microstructures. Porous ZnO nanoplates were synthesized by combining a microwave-assisted route with a calcination process and the gas sensing properties have been investigated.[51] Zhang et al. reported a solvothermal route to synthesize hierarchically porous ZnO using ethanol as solvent with the assistance of hexamethylenetetramine (HMT).[52] 3D porous architectures with multilayered ZnO nanosheets were obtained through a two-step approach, which contains the preparation of precursor from zinc acetate and urea, and then the calcination of precursor.[50] The experimental results indicated that the 3D ZnO porous structures exhibited the enhanced gas sensing properties than those of nanosheets and commercial ZnO powders. Although the sensitivity has been improved due to the porous structures, the response and recovery time is still a limited factor for gas sensing materials. Many strategies have been proposed to improve the sensitivity and shorten the response and recovery time of ZnO gas sensor. Liu et al. reported the synthesis of 3D hierarchical ZnO porous structures functionalized by Au.[53] Fe-doped ZnO porous nanosheets were prepared to enhance gas sensing property.[54] Au or Fe doping improved the gas sensing properties of ZnO in

Received: October 26, 2011
Accepted: January 4, 2012
Published: January 4, 2012

terms of high sensitivity and fast response at the cost of a complicated and uneconomic process. In addition, the above synthesis routes can prepare porous ZnO structures, but they usually exhibit weak dispersity and broad size distribution, which will affect their practical applications. Therefore, it is still a challenge to find new efficient routes to synthesize monodispersed 3D ZnO porous architectures for various applications. It is believed that the gas sensing properties including the sensitivity and the response and recovery times are related to gas diffusion and mass transport. 3D ZnO porous architectures with hierarchically 2D nanosheets may provide abundant passageway for gas absorption and desorption, and thus both high porosity and loosely layered microstructure of materials are important to gas sensing properties.

Herein, we report a facile approach to prepare nestlike 3D porous ZnO with hierarchically 2D lamellar structures, in which the $Zn_5(CO_3)_2(OH)_6$ precursor is prepared by a hydrothermal process using zinc acetate and ammonium carbonate as the starting materials with the assistance of glycine, Na_2SO_4, and polyvinyl pyrrolidone (PVP). The 3D ZnO hierarchically porous structures were obtained by thermal-decomposing the $Zn_5(CO_3)_2(OH)_6$ precursor, and the morphology evolution was investigated on the base of the control experiments. The gas sensor testing results showed that the nestlike ZnO hierarchically porous structures displayed a superior gas sensing performance.

MATERIALS AND METHODS

Materials. All reactants were of analytical grade and used as received without any further purification. Zinc acetate ($Zn(CH_3COO)_2{\cdot}2H_2O$), glycine ($NH_2CH_2COOH$), ammonium carbonate ($(NH_4)_2CO_3$), sodium sulfate ($Na_2SO_4$), polyvinyl pyrrolidone (PVP) and absolute ethyl alcohol (CH_3CH_2OH) were purchased from Sinopharm Chemical Reagent Co., Ltd.

Synthesis of Nestlike 3D Porous ZnO with Hierarchically 2D Nanoflakes. In a typical process, 0.5 g PVP were dissolved in 30 mL of deionized water, followed the addition of 0.22 g of $Zn(CH_3COO)_2{\cdot}2H_2O$, 0.2 g of glycine, and 0.2 g of Na_2SO_4 under magnetic stirring to form a mixed solution. Then, 20 mL of deionized water solution with 0.19 g of $NH_3)_2CO_3$ was dropped into the above mixed solution under magnetic stirring, and a transparent solution was obtained. After being stirred for 10 min, the resultant solution was transferred into a Teflon-lined stainless-steel autoclave with volume of 100 mL, and subsequently sealed and heated at 180 °C for 2 h. The white product was centrifuged and washed with deionized water and ethanol for five times, respectively, and then dried in an oven at 60 °C for 10 h for further experiments and characterizations. Porous ZnO was obtained by annealing the as-prepared precursors at 450 °C for 2 h. In the hydrothermal synthesis process, PVP was used to control the morphology. To further reveal the formation process of the nestlike $Zn_5(CO_3)_2(OH)_6$ hierarchically structures in the hydrothermal reaction, we carried out a series of experiments by varying the reaction time and temperature.

Characterizations and Gas Sensing Measurements. X-ray powder diffraction (XRD) pattern was obtained by a Rigaku Dmax-rc X-ray diffractometer with Ni filtered Cu Kα radiation (V = 40 kv, I = 50 mA) at a scanning rate of 4° min^{-1}. The microstructures of the resultant products were examined using a JSM-6700F field emission scanning electron microscope (FE-SEM) at an accelerating voltage of 20 kV and electric current of 1.0×10^{-10}A, and a JEOL JEM-2100 high-resolution TEM (HR-TEM) operated at 200 kV. Fourier transform infrared spectrometer (FTIR) was recorded on a VERTEX-70 FT-IR spectrometer. Thermogravimetric (TG) and differential thermal analysis (DTA) were performed on a diamond TG/DTA Perkin-Elmer instrument at a heating rate of 10 °C min^{-1} under air flux in the temperature ranging from 30 to 600 °C. The N_2 adsorption/desorption isotherms of ZnO porous structures were measured at 77 K on a Quadrasorb-SI instrument. The specific surface area was calculated by N_2 physisorption (S_{BET}) and the pore size distribution was calculated by the density functional theory (DFT) method. The gas sensor properties of the porous ZnO were tested on a HW-30A gas sensitivity instrument (HanWei Electronics Co., Ltd., Henan, China). The fabrication and testing principle of gas sensor refers to previous works.[50−52] The tested gas was injected into a glass chamber by a microsyringe and mixed with air. The sensitivity of the samples was defined as the ratio of R_a/R_g, where R_a and R_g are the electrical resistance of the sensor in air and in test gas, respectively.

RESULTS AND DISCUSSION

The phase and purity of $Zn_5(CO_3)_2(OH)_6$ precursor and nestlike 3D ZnO porous structures were investigated by XRD. As shown in Figure 1a, all diffraction peaks can be indexed to

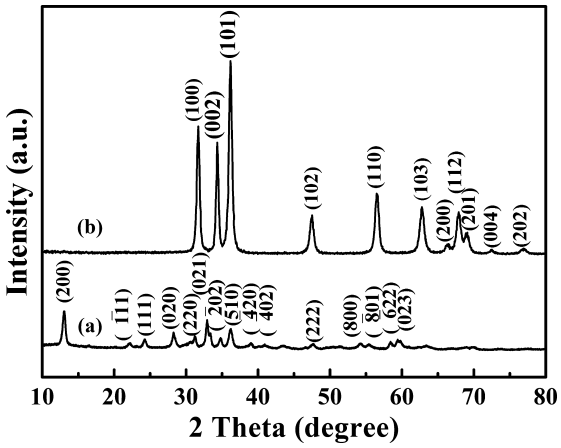

Figure 1. XRD patterns of (a) $Zn_5(CO_3)_2(OH)_6$ precursor and (b) nestlike 3D ZnO porous structures after thermal-decomposing the $Zn_5(CO_3)_2(OH)_6$ precursor at 450 °C for 2 h.

the monoclinic hydrozincite $Zn_5(CO_3)_2(OH)_6$ (JCPDS 19−1458), and no any peak of other phase is detected, suggesting the high purity of $Zn_5(CO_3)_2(OH)_6$ precursor prepared in this hydrothermal process. After being annealed at 450 °C for 2 h, the characteristic peaks of XRD pattern (Figure 1b) could match well with hexagonal wurtzite ZnO (JCPDS 36−1451), and no any diffraction peak from $Zn_5(CO_3)_2(OH)_6$ was observed, indicating that the $Zn_5(CO_3)_2(OH)_6$ precursor has been transformed into ZnO completely.

The thermal behaviors of the $Zn_5(CO_3)_2(OH)_6$ precursor have been examined by TG and DTA analysis. As present in Figure 2, the total weight loss was determined to be ca. 25.3 wt %,

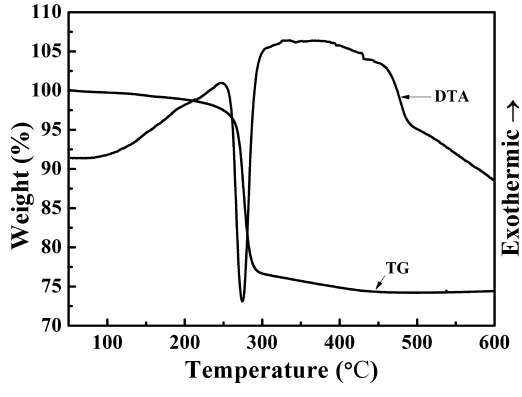

Figure 2. TG and DTA curves of $Zn_5(CO_3)_2(OH)_6$ precursor.

approaching to the theoretical value (25.96 wt %) of the decomposition of $Zn_5(CO_3)_2(OH)_6$. The weight loss at low temperature (below 200 °C) was mainly attributed to the removal of absorbed water on the sample surface. After that, a drastic decrease in the dominant weight loss profile between 250 and 300 °C demonstrates a rapid decomposition process of $Zn_5(CO_3)_2(OH)_6$ to ZnO, CO_2, and H_2O. A predominantly endothermic DTA peak appeared at around 278 °C, also suggesting the decomposition of $Zn_5(CO_3)_2(OH)_6$. In addition, the completion temperature of thermal-decomposing is about 450 °C, and thus it was chosen as the calcination temperature to prepare porous ZnO structures.

To complement the XRD and TG/DTA analysis, FT-IR was performed for the $Zn_5(CO_3)_2(OH)_6$ precursor and porous ZnO structures in an IR detection range of 400−4000 cm^{-1}. In Figure 3a, the FT-IR spectrum of $Zn_5(CO_3)_2(OH)_6$ precursor

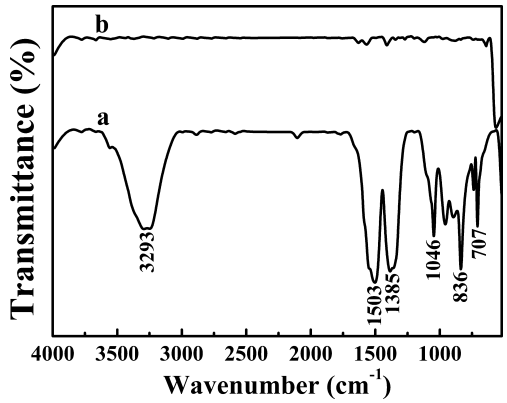

Figure 3. FT-IR spectra of (a) $Zn_5(CO_3)_2(OH)_6$ precursor and (b) the obtained nestlike 3D ZnO porous structures.

showed that a broad peak at 3293 cm^{-1} was assigned to hydroxyl groups and water molecules, and the bands around 1503, 1385, 836, and 707 cm^{-1} could be attributed to the C−O bending vibration of CO_3^{2-}.[50,52] After being annealed at 450 °C for 2 h, the FT-IR measurement (Figure 3b) confirmed the formation of ZnO based on the disappearance of the O−H (3293 cm^{-1}) and C−O (1503, 1385, 836, and 707 cm^{-1}) vibration modes. The $Zn_5(CO_3)_2(OH)_6$ precursor reacted with oxygen to form volatile species such as CO_2 and H_2O leaving behind the porous ZnO structures, which are in good agreement with the results of XRD and TG/DTA measurements.

From the panoramic SEM image (Figure 4a), $Zn_5(CO_3)_2(OH)_6$ precursor formed 3D nestlike architectures with size of 1.0−3.0 μm. Close inspection reveals that the precursor architectures are built of 2D nanoflakes (Figure 4b), which assemble with each other to form the three-dimensional nestlike structures, and the thickness of nanoflake is ca. 20 nm. The as-prepared architectures are very stable, and even two hours of ultrasonication cannot break them into discrete flakes, indicating that the nestlike architectures are integrative. After being annealed in air for 2 h, the as-prepared $Zn_5(CO_3)_2(OH)_6$ precursor was completely decomposed to phase-pure hexagonal wurtzite ZnO (Figure 1b). From the panoramic SEM image (Figure 4c), the primary morphologies of $Zn_5(CO_3)_2(OH)_6$ intermediates were reserved well, while the higher magnification image for individual particle (Figure 4d) shows that ZnO remained a intact 3D framework with porous structures after CO_2 and H_2O released during the thermal decomposition. To further reveal the porous structures, HR-TEM characterizations were performed on the nestlike ZnO architectures (Figure 5). The apparent contrast between the white part and the black ligaments also confirms the nanoporous wormhole-like characteristic (Figure 5b), and the pore size is ca. 3−40 nm. The corresponding selected area electron diffraction (SAED) pattern (Figure 5d) presents a polycrystalline nature of the porous structures. From the higher magnification HR-TEM image (Figure 5c), the typical lattice fringe spacing was measured to be 0.256 nm, corresponding to the (002) crystal plane of hexagonal wurtzite ZnO.

In addition to microstructure, the porosity and surface area of materials are important to gas sensing properties, and thus BET N_2 adsorption−desorption analysis was carried out on the nestlike ZnO porous architectures. The nitrogen adsorption/desorption isotherms shown in Figure 6 are ascribed to type H3 with large hysteresis loops, suggesting the presence of mesopores in the nestlike ZnO architectures. The calculated pore size distribution using BJH method indicated that the size of mesopores is not uniform ranging from 3 to 40 nm (inset in Figure 6), which is consistent with the HR-TEM observation (Figure 5b). The BET surface area of the nestlike ZnO porous architectures was 36.4 $m^2\ g^{-1}$, which was larger than that of 3D ZnO structures (23 $m^2\ g^{-1}$) and ZnO nanoplates (15.9 $m^2\ g^{-1}$).[50,51] Polarz et al.[55] reported that the ordered mesoporous ZnO prepared on the mesoporous carbon matrix has a high surface area of 200 $m^2\ g^{-1}$, which is higher than the present nestlike ZnO porous architectures attributing to the fact that the building blocks of nestlike ZnO architectures are nanoflakes and the pores imbedded in the nanoflakes cannot generate too much inner surface area.

To investigate the formation process of the nestlike $Zn_5(CO_3)_2(OH)_6$ precursor, we carried out a series of experiments by varying the reaction time and temperature, respectively. The time-dependent experiments demonstrate that the formation of 3D nestlike structures is a step-by-step process. SEM images of $Zn_5(CO_3)_2(OH)_6$ at different reaction time and temperature were displayed in Figure 7. When the reaction temperature increased to 60 °C, a white precipitate was obtained. As shown in Figure 7a, the precipitate contains a lot of monodispered spheres with the diameter of ca. 3 μm agglomerating from tiny particles to reduce the surface energy. The spheres have a rough surface and a hole in the center. With the reaction temperature rising to 90 °C, thin slices began to form on the surface of the sphere particles. The thin slices grew gradually with the reaction temperature increasing to 180 °C, and the nestlike morphology was observed (Figure 7c). When the reaction was maintained at 180 °C for 60 min, the growth of thin slices at the expense of adjacent smaller slices/nanoparticles and the metastable crystallites form nanoflakes with better crystallization (Figure 7d), which can be referred to the Ostwald ripening process.[56,57] Further prolonging the reaction time to 120 min, more uniform well-defined nestlike architectures composed of nanoflakes were obtained. The microstructure and size had no obvious variation when the reaction time was further increased to 20 h in comparison with the sample produced after 2 h reaction (Figure 7f).

To investigate the effect of PVP on the final morphology, we performed the control experiment in the absence of PVP, whereas the other experimental parameters were kept. Experimental results showed that the nestlike $Zn_5(CO_3)_2(OH)_6$ architectures cannot be obtained in addition to a lot of spheres particles (2−3 μm) constructing by thin slices as shown in

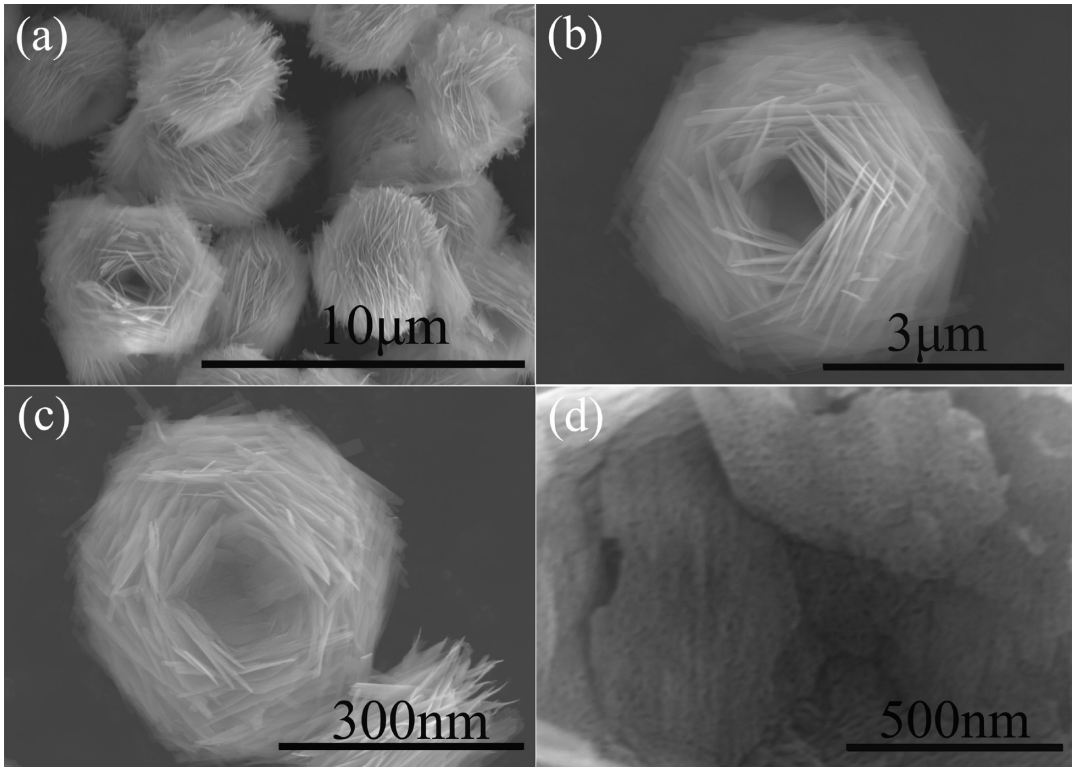

Figure 4. (a, b) SEM images of $Zn_5(CO_3)_2(OH)_6$ precursor, and (c, d) SEM images of nestlike 3D ZnO porous structures.

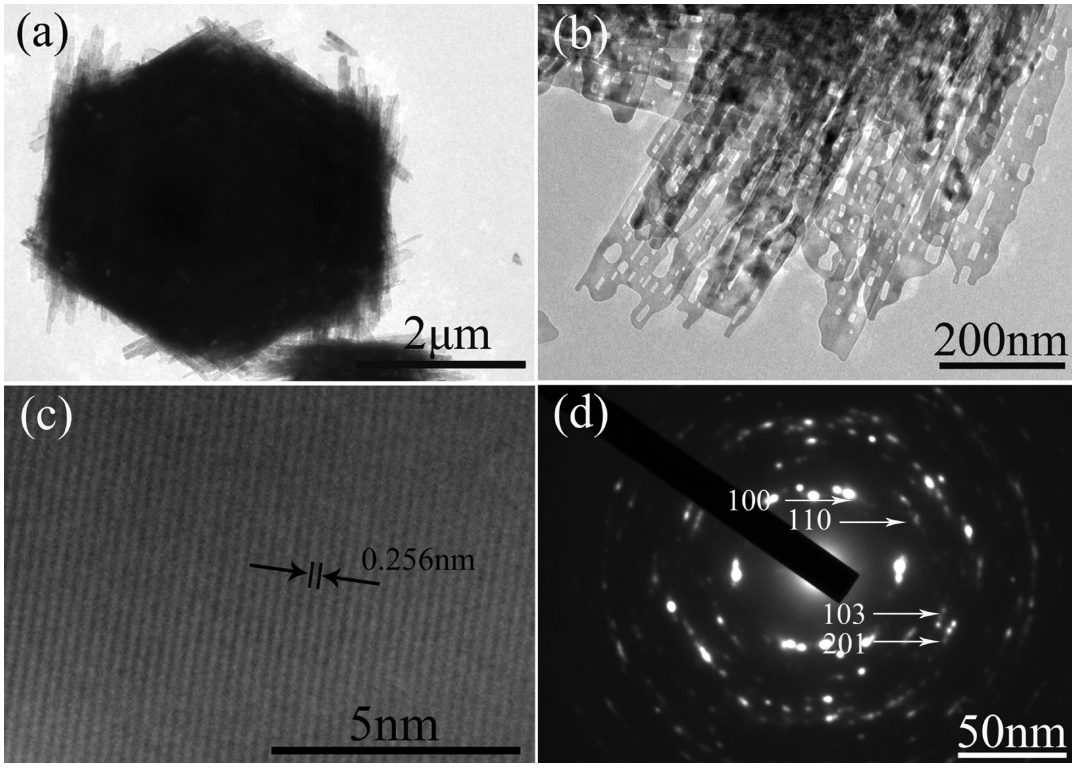

Figure 5. (a,b) TEM images, (c) HR-TEM image, and (d) SAED pattern of nestlike 3D ZnO porous structures.

Figure 8a, b. In the control experiments, we also investigated the effect of PEG and CTAB surfactants on the morphology of $Zn_5(CO_3)_2(OH)_6$ structures. When 0.5 g of PEG and 0.5 g of CTAB were added in the reaction, respectively, the messy clusters of nanoflakes with a wide size distribution were obtained in addition to a few of nestlike architectures (Figure 8c, d). It is believed that PVP played an important role in the formation of $Zn_5(CO_3)_2(OH)_6$ nestlike morphology feature although the exact influence mechanism is not clear. The influence of PVP on the growth mechanism of nestlike $Zn_5(CO_3)_2(OH)_6$ architectures is planned to study in the future.

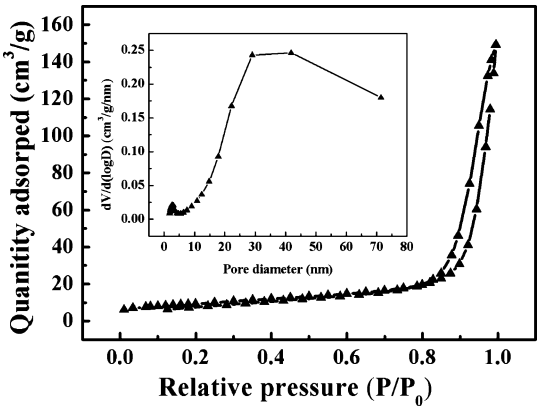

Figure 6. Nitrogen adsorption/desorption isotherms of nestlike 3D ZnO porous structures. The inset is pore size distribution.

In this work, we also found that the morphology of final product depends on the addition of Na_2SO_4. The messy clusters of nanoflakes with a wide size distribution were obtained without Na_2SO_4 doping (see Figure 9), while the well-defined $Zn_5(CO_3)_2(OH)_6$ nestlike architectures with smooth nanoflakes generated when 0.2 g of Na_2SO_4 was added to the reaction system. Previous investigations confirmed that the inorganic soluble salts as complexing agent added in solution can inhibit the deposition of crystallites,[58,59] and therefore, the deposition rate of Zn^{2+} decreased through the addition of Na_2SO_4 in favor of the growth of monodispersed nestlike architectures due to the strong coordination of SO_4^{2-} to Zn^{2+} in this reaction system. In the present study, a clear transparent solution was obtained when $(NH_4)_2CO_3$ solution was dropped into zinc acetate aqueous solution. If without Na_2SO_4 addition, the white precipitate will produce after the doping of zinc acetate into ammonium carbonate aqueous solution, corresponding to the previous work.[60]

The reactions for the formation of nestlike ZnO porous architectures can be illustrated as follows[60]

$$Zn^{2+} + 2gly \rightarrow Zn(gly)_2^{2+} \quad (1)$$

$$(NH_4)_2CO_3 \rightarrow 2NH_4^+ + CO_3^{2-} \quad (2)$$

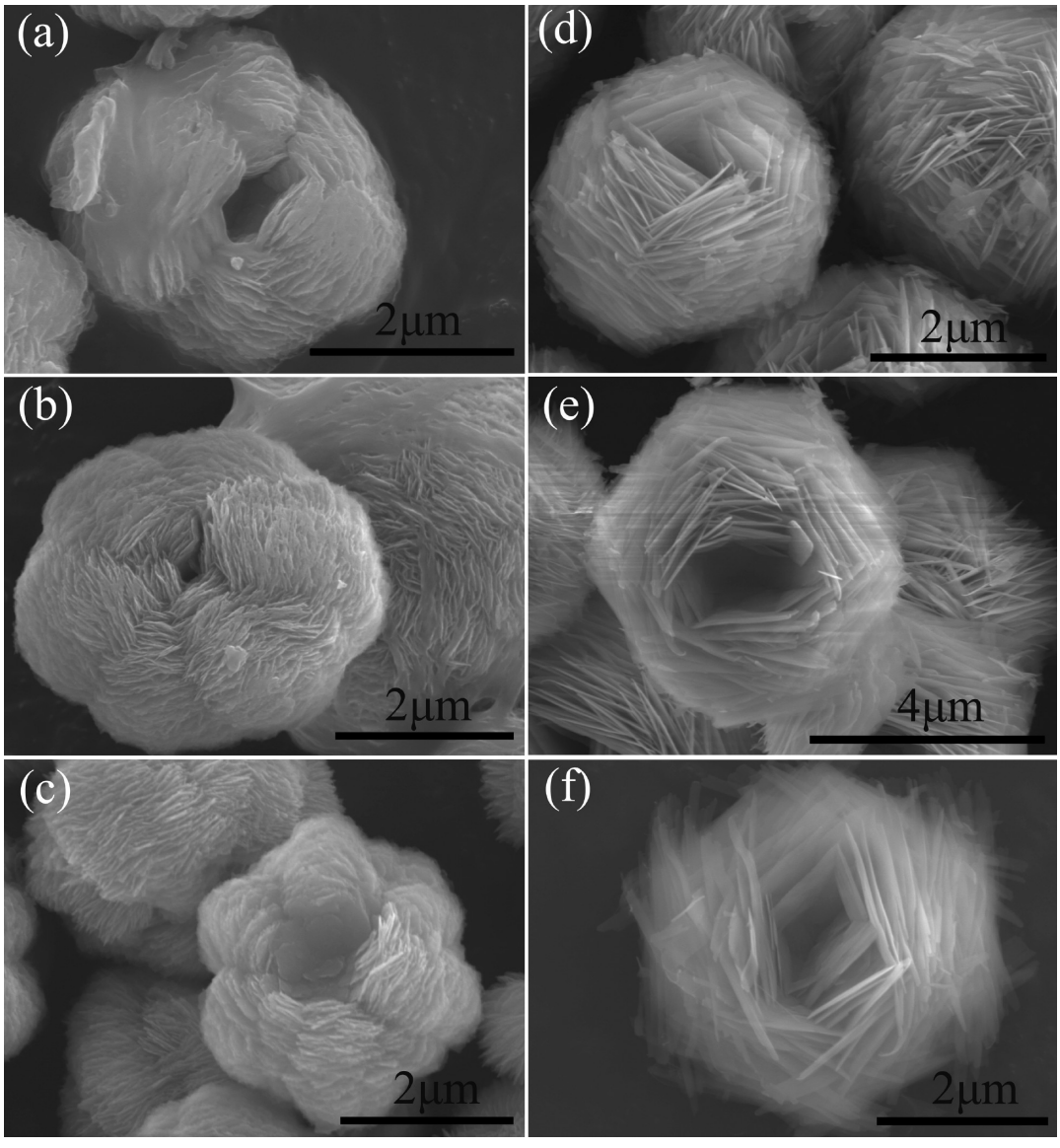

Figure 7. SEM images of the precursors prepared at different temperature and reacted for different time: (a) 60 °C, 0 h, (b) 90 °C, 0 h, (c) 180 °C, 0 h, (d) 180 °C, 1 h, (e) 180 °C, 2 h, and (f) 180 °C, 20 h.

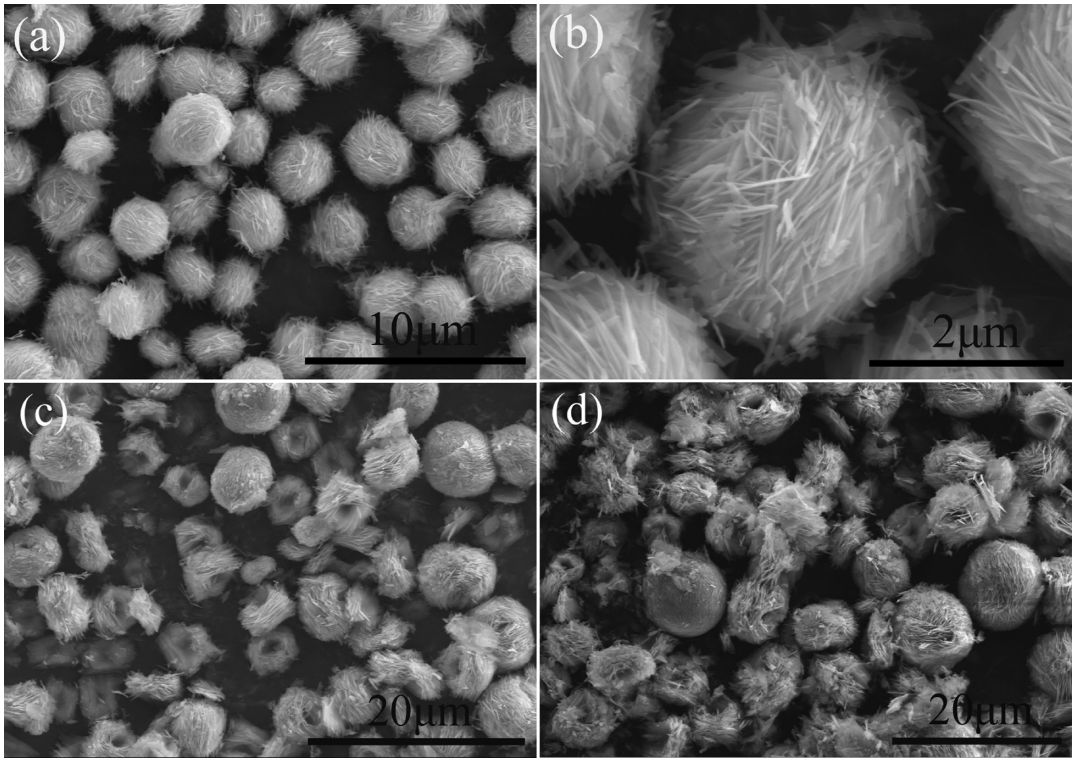

Figure 8. SEM images of $Zn_5(CO_3)_2(OH)_6$ precursor prepared (a, b) without the addition of PVP, (c) with 0.5 g CTAB addition, and (d) with 0.5 g PEG addition.

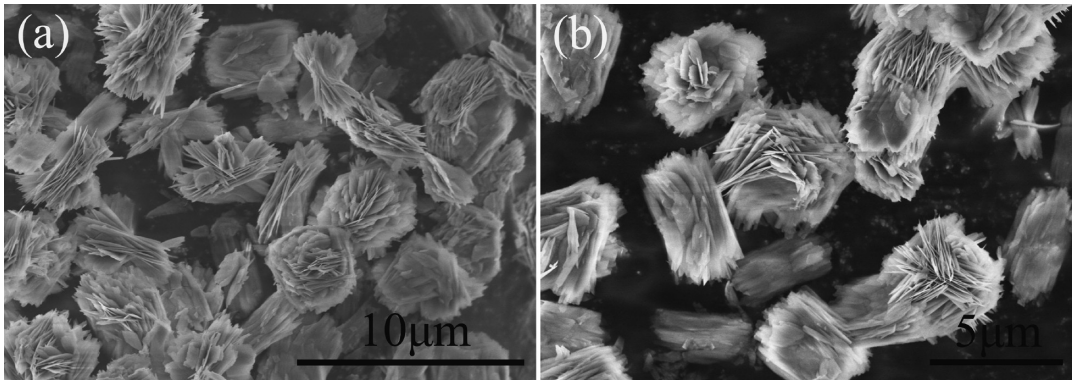

Figure 9. (a, b) SEM images of $Zn_5(CO_3)_2(OH)_6$ precursor fabricated in the absence of Na_2SO_4 at different magnification.

$$5Zn(gly)_2^{2+} + 2CO_3^{2-} + 6OH^- \rightarrow Zn_5(OH)_6(CO_3)_2 + 10gly \quad (3)$$

$$Zn_5(OH)_6(CO_3)_2 \rightarrow 5ZnO + 2CO_2 \uparrow + 3H_2O \quad (4)$$

First, Zn^{2+} ions combined with glycine to form $Zn(gly)_2^{2+}$ in the aqueous solution under stirring. In the hydrothermal condition, $(NH_4)_2CO_3$ was decomposed to NH_4^+ and CO_3^{2-} in aqueous solution. With the progress of reaction, $Zn_5(CO_3)_2(OH)_6$ precursor was formed by the reaction of zinc glycinate complex with carbonate and hydroxyl under a hydrothermal condition. Finally, porous ZnO was obtained after the thermal decomposition of $Zn_5(CO_3)_2(OH)_6$ precursor.

It is known that the sensitivity of ZnO gas sensor is mainly related to operating temperature and gas concentration. To study the gas sensor properties of the nestlike 3D porous ZnO with hierarchically 2D nanoflakes, series of experiments were carried out by varying the operating temperature and gas concentration, respectively. The sensitivity of the nestlike 3D porous ZnO with hierarchically 2D nanoflakes exposed to ethanol and acetone at different temperatures were shown in Figure 10. The response sensitivity of both gases varied with the operating temperature. The sensitivity increased between 240 to 420 °C, and then decreased with increasing the operating temperature. The maximum sensitivity values of 12.2 and 17.4 were obtained at 420 °C for ethanol and acetone, respectively. For the messy clusters of nanoflakes (shown in Figure 9), the maximum sensitivity values decreased to 9.9 and 15.0 for ethanol and acetone. Figures 11 and 12 show the dynamic response and recovery curves of the nestlike 3D porous ZnO with hierarchically 2D nanoflakes as the ethanol and acetone gas sensor, respectively, and the operating temperature is 420 °C. From the above measured results, the sensors have a wide detection range from 5 to 1000 ppm for both ethanol and acetone, and the response amplitude of the two sensors

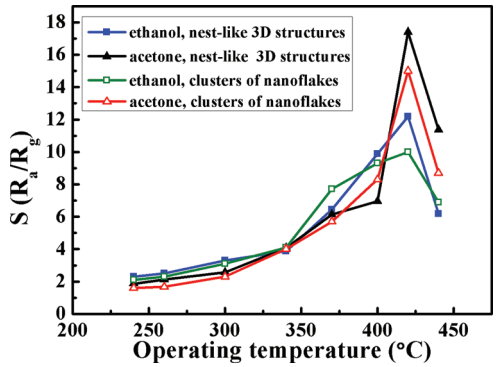

Figure 10. Gas sensitivities measured at different operating temperatures to 100 ppm ethanol and acetone.

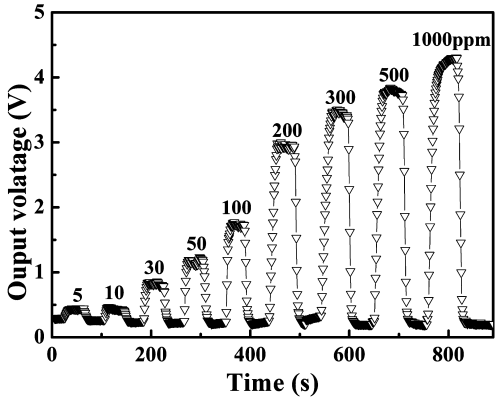

Figure 11. Dynamic response curve of the sensor prepared from nestlike 3D ZnO porous structures to ethanol with concentrations ranging from 5 to 1000 ppm and at the operating temperature of 420 °C.

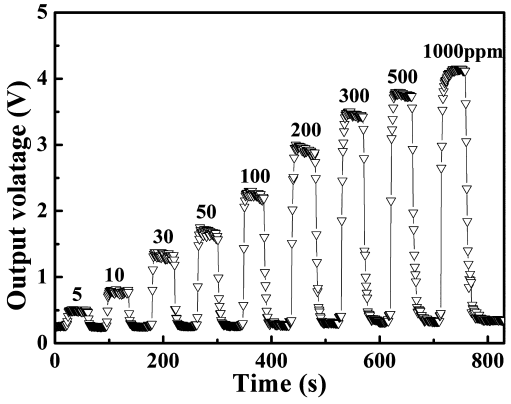

Figure 12. Dynamic response curve of the sensor prepared from nestlike 3D ZnO porous structures to acetone with concentrations ranging from 5 to 1000 ppm and at the operating temperature of 420 °C.

increases with the gas concentration. The sensitivity is plotted as a function of gas concentration in Figure 13. The sensitivity is proportional to the concentration of ethanol or acetone, and the gas sensor is more sensitive to acetone than ethanol from 5 to 100 ppm. When the concentration of ethanol increased to 200 ppm, the sensitivity of the gas sensor jumps to 37, and exceeds the sensitivity (ca. 25) to acetone at the same concentration. The unique nestlike 3D porous ZnO architectures provide high response sensitivity to acetone at low concentration,

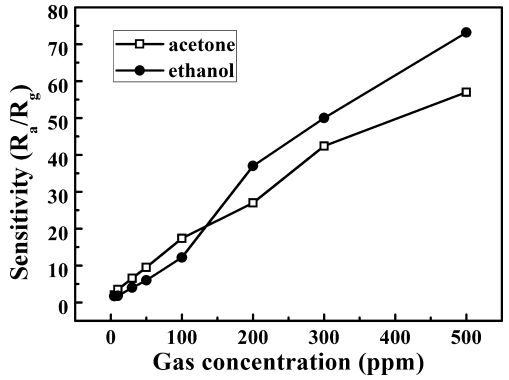

Figure 13. Sensitivities of the sensor prepared from nestlike 3D ZnO porous structures versus different ethanol and acetone concentrations.

and a good sensor to ethanol at relatively higher concentration. For 100 ppm ethanol, the sensitivity of 12.2 is about three times higher than the sensor reported previously.[52] In addition, the response and recovery speeds are also the key factors for the gas sensor applications, and thus the response and recovery times were measured when 100 ppm testing gas was introduced. In this work, the response and recovery times of the nestlike 3D porous ZnO architectures were 9 and 8 s for ethanol, respectively. The response time was prolonged with the increase of ethanol concentration, but the recovery time was kept the same for various concentrations. The response and recovery times are much shorter than those (32 and 17 s) of the sensor prepared by ZnO nanoplates.[51] For 100 ppm acetone, the response and recovery times were 5 and 7 s, respectively, which are shorter than the response and recovery times (5 and 28 s) for the sensor fabricated by 3D ZnO porous architectures,[50] indicating the high response and recovery speeds for the sensor made from the nestlike 3D ZnO porous architectures.

The mechanism of ZnO gas sensor has been presented in the previous works.[50,51,61] For the gas sensor fabricated from the nestlike 3D porous ZnO with hierarchically 2D nanoflakes, the voids and interspaces existing among nanoflakes facilitate the gas adsorption and desorption, and porous nanoflakes provide large contacting surface area with more reactive sites for electrons, oxygen and target gas. In addition, the network of interconnected pores and voids in sensor films fabricated from the nestlike 3D porous ZnO architectures provided abundant channels for gas diffusion and mass transport in comparison with the compact ZnO structures, also resulting in the sensing property enhancements. Therefore, the unique nestlike 3D porous ZnO architectures with high porosity and large surface area are critically important to shorten the response and recovery times, and to enhance the sensitivity of gas sensors.

CONCLUSIONS

In present work, nestlike 3D ZnO hierarchically porous structures have been successfully synthesized by a hydrothermal approach combining with a subsequent calcination process. The formation process of nestlike ZnO porous structures has also been investigated on the base of experiment results. The unique nestlike 3D porous ZnO with hierarchically 2D nanoflakes provides large contacting surface area with more reactive sites for electrons, oxygen ions and target gas and abundant channels for gas diffusion and mass transport, resulting in the excellent gas sensing performances including high sensitivity and short response and recovery times.

dx.doi.org/10.1021/am201476b | ACS Appl. Mater. Interfaces 2012, 4, 817–825

AUTHOR INFORMATION

Corresponding Author
*E-mail: jrliu@sdu.edu.cn.

ACKNOWLEDGMENTS

This work was supported by the grant for Qi-Lu Young Scholar program and Independent Innovation Foundations of Shandong University (2009JQ015, 2009TB010). The authors also acknowledge the financial supports from National Natural Science Foundation (21071090), the Research Fund for the Doctoral Program of Higher Education of China (20090131120032, 20100131120026), the Excellent Young Scientist Fund of Shandong Province (BS2009CL040, BS2010CL032), the New Century Excellent Talent Program (NCET-10-0545) and the Returned Overseas Chinese Scholars, State Education Ministry.

REFERENCES

(1) Zhang, G. k.; Shen, X.; Yang, Y. Q. *J. Phys. Chem. C* **2011**, *115*, 7145−7152.
(2) Tiemann, M. *Chem.—Eur. J.* **2007**, *13*, 8376−8388.
(3) Du, N.; Zhang, H.; Chen, B.; Ma, X.; Liu, Z.; Wu, J.; Yang, D. *Adv. Mater.* **2007**, *19*, 1641−1645.
(4) Sun, C. W.; Rajasekhara, S.; Goodenough, J. B.; Zhou, F. *J. Am. Chem. Soc.* **2011**, *133*, 2132−2135.
(5) Liu, J.; Xia, H.; Lu, L.; Xue, D. F. *J. Mater. Chem.* **2010**, *20*, 1506−1510.
(6) Wang, H. E.; Zheng, L. X.; Liu, C. P.; Liu, Y. K.; Luan, C. Y.; Cheng, H.; Li, Y. Y.; Martinu, L.; Zapien, J. A.; Bello, I. *J. Phys. Chem. C* **2011**, *115*, 10419−10425.
(7) Liu, J. Y.; Luo, T.; T, S. M.; Meng, F.; Sun, L. B.; Li, M. Q.; Liu, J. H. *Chem. Commun.* **2010**, *46*, 472−474.
(8) Wan, Y.; Zhao, D. Y. *Chem. Rev.* **2007**, *107*, 2821−2860.
(9) Yu, H. D.; Wang, D. S.; Han, M. Y. *J. Am. Chem. Soc.* **2007**, *129*, 2333−2337.
(10) Qian, L. H.; Yan, X. Q.; Fujita, T.; Inoue, A.; Chen, M. W. *Appl. Phys. Lett.* **2007**, *90*, 153120.
(11) Chen, L. F.; Song, Z.; Wang, X.; Prikhodko, S. V.; Hu, J. C.; Kodambaka, S.; Richards, R. *ACS Appl. Mater. Interfaces* **2009**, *9*, 1931−1937.
(12) Wan, Q.; Li, Q. H.; Chen, Y. J.; Wang, T. H. *Appl. Phys. Lett.* **2004**, *18*, 3654−3656.
(13) Wang, N.; Cao, X.; Wu, Q. Y.; Zhang, R.; Wang, L.; Yin, P.; Guo, L. *J. Phys. Chem. C* **2009**, *113*, 21471−21476.
(14) Wang, X. D.; Song, J. H.; Liu, J.; Wang, Z. L. *Science* **2007**, *316*, 102−105.
(15) Gao, P. X.; Song, J. H.; Liu, J.; Wang, Z. L. *Adv. Mater.* **2007**, *19*, 67−72.
(16) Lao, C. S.; Li, Y.; Wong, C. P.; Wang, Z. L. *Nano Lett.* **2007**, *7*, 1323−1328.
(17) Lee, S. W.; Jeong, M. C.; Myoung, J. M.; Chae, G. S.; Chung, I. J. *Appl. Phys. Lett.* **2007**, *90*, 133115.
(18) Fan, Z. Y.; Dutta, D.; Chien, C. J.; Chen, H. Y.; Brown, E. C.; Chang, P. C.; Lu, J. G. *Appl. Phys. Lett.* **2006**, *89*, 213110.
(19) Martinson, A. B. F.; Elam, J. W.; Hupp, J. T.; Pellin, M. J. *Nano Lett.* **2007**, *7*, 2183−2187.
(20) Qiu, J. H.; Guo, M.; Wang, X. D *ACS Appl. Mater. Interfaces* **2011**, *3*, 2358−2367.
(21) Bera, A.; Ghosh, T.; Basak., D. *ACS Appl. Mater. Interfaces* **2010**, *2*, 2898−2903.
(22) Bagnall, D. M.; Chen, Y. F.; Zhu, Z.; Yao, T.; Koyama, S.; Shen, M. Y.; Goto, T. *Appl. Phys. Lett.* **1997**, *17*, 2230−2232.
(23) Tsukazaki, A.; Ohtomo, A.; Onuma, T.; Ohtani, M.; Makino, T.; Sumiya, M.; Ohtani, K.; Chichibu, S. F.; Fuke, S.; Segawa, Y.; Ohno, H.; Koinuma, H.; Kawasaki, M. *Nat. Mater.* **2005**, *4*, 42−46.
(24) Lupan, O.; Pauporté, T.; Viana, B.; Tiginyanu, I. M.; Ursaki, V. V.; Cortès, R. *ACS Appl. Mater. Interfaces* **2010**, *2*, 2083−2090.
(25) Yang, J. L.; An, S. J.; Park, W. I.; Yi, G. C.; Choi, W. Y. *Av. Mater.* **2004**, *16*, 1661−1664.
(26) Zhang, L. Y.; Yin, L. W.; Wang, C. X.; Lun, N.; Qi, Y. X. *ACS Appl. Mater. Interfaces* **2010**, *2*, 1769−1773.
(27) Tang, Z. K.; Wong, G. K. L.; Yu, P.; Kawasaki, M.; Ohtomo, A.; Koinuma, H.; Segawa, Y. *Appl. Phys. Lett.* **1998**, *25*, 3270−3272.
(28) Guo, Z. H.; W, S. Y.; Shedd, B.; Scaffaro, R.; Pereira, T.; Haha, H. T. *J. Mater. Chem* **2007**, *17*, 806−813.
(29) Yao, K. X; Zeng, H. C *J. Phys. Chem. C* **2007**, *111*, 13301−13308.
(30) Wang, X. D.; Summers, C. J.; Wang, Z. L. *Nano Lett.* **2004**, *3*, 423−426.
(31) Yang, P. D.; Yan, H. Q.; Mao, S.; Russo, R.; Johnson, J.; Saykally, R.; Morris, N.; Pham, J.; He, R. R.; Choi, H. J. *Adv. Funct. Mater.* **2002**, *12*, 323−331.
(32) Xing, Y. J.; Xi, Z. H.; Xue, Z. Q.; Zhang, X. D.; Song, J. H. *Appl. Phys. Lett.* **2003**, *9*, 1689−1691.
(33) Park, W. I.; Yi, G. C.; Kim, M.; Pennycook, S. J. *Adv. Mater.* **2002**, *24*, 1841−1843.
(34) Kong, X. Y.; Wang, Z. L. *Appl. Phys. Lett.* **2004**, *6*, 975−977.
(35) Park, J. H.; Choi, H. J.; Choi, Y. J.; Sohn, S. H.; Park, J. G. *J. Mater. Chem.* **2004**, *14*, 35−36.
(36) Zhang, Y.; Xu, J. Q.; Xiang, Q.; Li, H.; Pan, Q. Y.; Xu, P. C. *J. Phys. Chem. C* **2009**, *113*, 3430−3435.
(37) Fang, Z.; Tang, K. B.; Shen, G. Z.; Chen, D.; Kong, R.; Lei, S. J. *Mater. Lett.* **2006**, *60*, 2530−2533.
(38) Jang, J. M.; Kim, C. R.; Ryu, H.; Razeghi, M.; Jung, W. G. *J. Alloys Compd.* **2008**, *463*, 503−510.
(39) Sinha, A. K.; Basu, M.; Pradhan, M.; Sarkar, S.; Pal, T. *Chem.—Eur. J.* **2010**, *16*, 7865−7874.
(40) Gao, X. F.; Jiang, L. *Nature* **2004**, *432*, 36.
(41) Mao, Y.; Kanungo, M.; Hemraj-Benny, T. H.; Wong, S. S. *J. Phys. Chem. B* **2006**, *110*, 702−710.
(42) Huang, J. R.; Wu, Y. J.; Gu, C. P.; Zhai, M. H.; Sun, Y. F.; Liu., J. H. *Sens. Actuators, B* **2011**, *155*, 126−133.
(43) Huang, X. H.; Xia, X. H.; Yuan, Y. F.; Zhou, F. *Electrochim. Acta* **2011**, *56*, 4960−4965.
(44) Wang, X. B.; Cai, W. P.; Lin, Y. X.; Wang, G. Z.; Liang, C. H. *J. Mater. Chem.* **2010**, *20*, 8582−8590.
(45) Liang, J. B.; Bai, S.; Zhang, Y. S.; Li, M.; Yu, W. C.; Qian, Y. T. *J. Phys. Chem. C* **2007**, *111*, 1113−1118.
(46) Chernikov, A.; Horst, S.; Waitz, T.; Tiemann, M.; Chatterjee, S. *J. Phys. Chem. C* **2011**, *115*, 1375−1379.
(47) Wang, J. X.; Wu, C. M. L.; Cheung, W. S.; Luo, L. B.; He, Z. B.; Yuan, G. D.; Zhang, W. J.; lee, C. S.; Lee., S. T. *J. Phys. Chem. C* **2011**, *114*, 13157−13161.
(48) Wang, H. Q.; Li, G. H.; Jia, L. C.; Wang, G. Z.; Tang, C. J. *J. Phys. Chem. C* **2008**, *112*, 11738−11743.
(49) Xu, F.; Zhang, P.; Navrotsky, A.; Yuan, Z. Y.; Ren, T. Z.; Halasa, M.; Su, B. L. *Chem. Mater.* **2007**, *19*, 5680−5686.
(50) Li, J.; Fan, H. Q.; Jia, X. H. *J. Phys. Chem. C* **2010**, *114*, 14684−14691.
(51) Jing, Z. H.; Zhan, J. H. *Adv. Mater.* **2008**, *20*, 4547−4551.
(52) Zhang, J.; Wang, S. R.; Xu, M. J.; Wang, Y.; Zhu, B. L.; Zhang, S. M. *Cryst. Growth Des.* **2009**, *8*, 3532−3537.
(53) Liu, X. H.; Zhang, J.; Wang, L. W.; Yang, T. L.; Guo, X. Z.; Wu, S. H.; Wang, S. R. *J. Mater. Chem.* **2011**, *21*, 349−356.
(54) Yu, A.; Qian, J. S.; Pan, H.; Cui, Y. M.; Xu, M. G.; Tu, L.; Chai, Q. L.; Zhou, X. F. *Sens. Actuators, B* **2011**, *158*, 9−16.
(55) Polarz, S.; Orlov, A. V.; Schuth, F.; Lu, A. H. *Chem.—Eur. J.* **2007**, *13*, 592−597.
(56) Lei, J.; Xu, L.; Morein, C.; Chen, C. H.; Lai, M.; Dharmarathna, S.; Dobley, A.; Suib, S. L. *Adv. Funct. Mater.* **2010**, *22*, 3373−3382.
(57) Kulak, A.; Iddon, P.; Li, Y. T.; Armes, S. P.; Colfen, H.; Paris, O.; Wilson, R. M.; Meldrum, F. C. *J. Am. Chem. Soc.* **2007**, *129*, 3729−3736.
(58) Wu, X. L.; Guo, Y. G.; Wan, L. J.; Hu, C. W. *J. Phys. Chem. C* **2008**, *112*, 16824−16829.

(59) Wang, X.; Yuan, F. L.; Hu, P.; Yu, L. J.; Bai, L. Y. *J. Phys. Chem. C* **2008**, *112*, 8773−8778.
(60) Xing, Z. J.; Geng, B. Y.; Li, X. L.; Jiang, H.; Feng, C. X.; Ge, T. *Cryst. Eng. Comm.* **2011**, *13*, 2137−2142.
(61) Gergintschew, Z.; Förster, H.; Kositza, J.; Schipanski, D. *Sen. Actuators, B* **1995**, *26*, 170−173.